

# Classification with an edge: improving semantic image segmentation with boundary detection

D. Marmanis<sup>a,c</sup>, K. Schindler<sup>b</sup>, J. D. Wegner<sup>b</sup>, S. Galliani<sup>b</sup>, M. Datcu<sup>a</sup>, U. Still<sup>a,c</sup>

<sup>a</sup> *DLR-IMF Department, German Aerospace Center, Oberpfaffenhofen, Germany – {dimitrios.marmanis, mihai.datcu}@dlr.de*

<sup>b</sup> *Photogrammetry and Remote Sensing, ETH Zurich, Switzerland – {konrad.schindler, jan.wegner, silvano.galliani}@geod.baug.ethz.ch*

<sup>c</sup> *Photogrammetry and Remote Sensing, TU München, Germany – stilla@tum.de*

## Abstract

We present an end-to-end trainable deep convolutional neural network (DCNN) for semantic segmentation with built-in awareness of semantically meaningful boundaries. Semantic segmentation is a fundamental remote sensing task, and most state-of-the-art methods rely on DCNNs as their workhorse. A major reason for their success is that deep networks learn to accumulate contextual information over very large receptive fields. However, this success comes at a cost, since the associated loss of effective spatial resolution washes out high-frequency details and leads to blurry object boundaries. Here, we propose to counter this effect by combining semantic segmentation with semantically informed edge detection, thus making class boundaries explicit in the model. First, we construct a comparatively simple, memory-efficient model by adding boundary detection to the SEGNET encoder-decoder architecture. Second, we also include boundary detection in FCN-type models and set up a high-end classifier ensemble. We show that boundary detection significantly improves semantic segmentation with CNNs in an end-to-end training scheme. Our best model achieves  $> 90\%$  overall accuracy on the ISPRS Vaihingen benchmark.

## 1. Introduction

Semantic image segmentation (a.k.a. landcover classification) is the process of turning an input image into a raster map, by assigning every pixel

to an object class from a predefined class nomenclature. Automatic semantic segmentation has been a fundamental problem of remote sensing data analysis for many years (Fu et al., 1969; Richards, 2013). In recent years there has been a growing interest to perform semantic segmentation also in urban areas, using conventional aerial images or even image data recorded from low-flying drones. Images at such high resolution (GSD 5-30 cm) have quite different properties. Intricate spatial details emerge like for instance road markings, roof tiles or individual branches of trees, which increase the spectral variability within an object class. On the other hand, the spectral resolution of sensors is limited to three or four broad bands so spectral material signatures are less distinctive. Hence, a large portion of the semantic information is encoded in the image texture rather than the individual pixel intensities, and much effort has gone into extracting features from the raw images that make the class information explicit (e.g. Franklin and McDermid, 1993; Barnsley and Barr, 1996; Dalla Mura et al., 2010; Tokarczyk et al., 2015).

At present the state-of-the-art tool for semantic image segmentation, in remote sensing as well as other fields of image analysis, are deep convolutional neural networks (DCNNs).<sup>1</sup> For semantic segmentation one uses so-called fully convolutional networks (FCNs), which output the class likelihoods for an entire image at once. FCNs have become a standard tool that is readily available in neural network software.

Why are DCNNs so successful (if given sufficient training data and computing resources)? Much has been said about their ability to learn the complete mapping from raw images to class labels (“end-to-end learning”), thus making heuristic feature design obsolete. Another strength is maybe even more important for their excellent performance: deep networks capture a lot of *context* in a tractable manner. Each convolution layer combines information from nearby pixels, and each pooling layer enlarges the footprint of subsequent convolutions in the input image. Together, this means that the output at a given pixel is influenced by a large spatial neighborhood. When the task is pixel-wise semantic segmentation<sup>2</sup>, their unparalleled ability to represent context however comes at a price. There is a trade-off between

---

<sup>1</sup>For example, the 15 best-performing participants in the *ISPRS Vaihingen* benchmark, not counting multiple entries from the same group, all use DCNNs.

<sup>2</sup>As opposed to, e.g., object recognition or speech recognition.

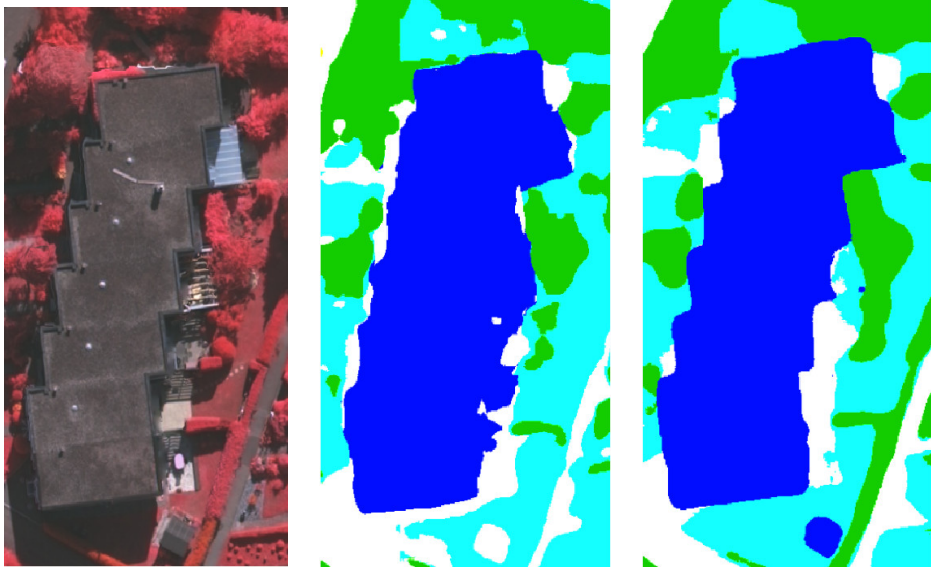


Figure 1: Semantic segmentation. Left: input image. Middle: DCNN segmentation, object boundaries tend to be blurred. Right: We propose to mitigate this effect by including an explicit object boundary detector in the network.

strong downsampling, which allows the network to see a large context, but loses high-frequency detail; and accurate localization of the object boundaries, which requires just that local detail. We note that in generic computer vision with close-range images that effect is much less critical. In a typical photo, say a portrait or a street scene, there are few, big individual objects and only few object boundaries, whose precise location moreover is only defined up to a few pixels. In some cases segmentation is even defined as finding the boundaries between very few (say,  $< 5$ ) dominant regions (Russell et al., 2009) that make up the image. On the contrary, for our remote sensing task we expect at least tens to hundreds of small segments, such as individual cars, trees, etc.

There has been some research that tries to mitigate the blurring of boundaries due to down-sampling and subsequent up-sampling, either by using the a-trous convolution (dilated convolution) (Yu and Koltun, 2016; Chen et al., 2016a; Sherrah, 2016) or by adding skip connections from early to deep layers of the network, so as to reintroduce the high-frequency detail after upsampling (Dosovitskiy et al., 2015; Badrinarayanan et al., 2017; Marmanis et al., 2016). Still, we find that when applied to remote sensing data with many

small objects, FCNs tend to blur object boundaries and visually degrade the result (see Fig.1).

In this paper, we propose to explicitly represent *class-boundaries* in the form of pixel-wise contour likelihoods, and to include them in the segmentation process. By class-boundaries we mean the boundaries between regions that have different semantic class, i.e., we aim for a “semantic edge-detection”. Our hypothesis is that if those boundaries, which by definition correspond to the location of the label transitions, are made available to the network, then it should learn to align the segmentation to them.

Importantly, recent work, in particular the *holistically nested edge detection* (HED [Xie and Tu, 2015](#); [Kokkinos, 2016](#)) has shown that edge detection can also be formulated as a FCN, reaching excellent results. We can therefore merge the two tasks into a single network, train them together and exploit synergies between them. The result is an end-to-end trainable model for semantic segmentation with a built-in awareness of semantically meaningful boundaries. We show experimentally that explicitly taking into account class boundaries significantly improves labeling accuracy, for our datasets up to 6%.

Overall, our boundary-aware ensemble segmentation network reaches state-of-the-art accuracy on the ISPRS semantic labeling benchmark. In particular, we find that adding boundary detection consistently improves the segmentation of man-made object classes with well-defined boundaries. On the contrary, we do not observe an improvement for vegetation classes, which have intrinsically fuzzy boundaries at our target resolution. Moreover, our experiments suggest that integrated boundary detection is beneficial both for light encoder/decoder architectures with comparatively few parameters like SEGNET, and for high-performance networks with *fully connected layers*, such as the VGG family, which are much heavier to train in terms of memory usage and computation time.

Our tests also confirm, perhaps unsurprisingly, that DCNNs perform optimally when merged into *ensemble models*. Combining multiple semantic segmentation networks seems beneficial to reduce the bias of individual models, both when using the same architecture with different initializations, and when using different model architectures with identical initializations.

In terms of practical relevance, a main message of this paper is that, with DCNNs, semantic segmentation is practically usable also for very high resolution urban remote sensing. It is typically thought that object extraction algorithms are good enough for (possibly semi-automatic) applications when

their predictions are at least 80% correct (Mayer et al., 2006). In our experiments, the  $F_1$ -score (harmonic mean between precision and recall) surpasses this threshold for all object classes, including small ones like cars. Frequent, well-defined man-made classes reach well above 90%.

## 2. Related Work

Semantic segmentation has been a core topic of computer vision as well as remote sensing for many years. A full review is beyond the scope of this paper, we refer the reader to textbooks such as (Szeliski, 2010; Richards, 2013). Here, we concentrate on methods that employ neural networks.

Even in the early phase of the CNN revival, semantic segmentation was tackled by Grangier et al. (2009). The study investigates progressively deeper CNNs for predicting pixel labels from a local neighborhood, and already shows very promising results, albeit at coarse spatial resolution. Socher et al. (2012) start their semantic segmentation pipeline with a single convolution and pooling layer. On top of that “feature extractor” they stack recursive neural networks (RNN), which are employed on local blocks of the previous layer in a rather convolutional manner. The RNNs have random weights, there is no end-to-end training. Notably, that work uses RGB-D images as input and processes depth in a separate stream, as we do in the present work. Related to this is the approach of Pinheiro and Collobert (2014), who use “recurrent CNNs”, meaning that they stack multiple shallow networks with tied convolution weights on top of each other, at each level using the predicted label maps from the previous level and an appropriately down-scaled version of the raw image as input. Farabet et al. (2013) train CNNs with 3 convolutional layers and a fully connected layer for semantic segmentation, then post-process the results with a CRF or by averaging over super-pixels to obtain a smooth segmentation. Like in our work, that paper generates an image pyramid and processes each scale separately with the CNN, but in contrast to our work the filter weights are tied across scales. An important milestone was the *fully convolutional network* (FCN) of Long et al. (2015). In that work it was shown that the final, fully connected layers of the network can be seen as a large stack of convolutions, which makes it possible to compute spatially explicit label maps efficiently. An further important work in this context is the *Holistically- Nested Edge Detection* (HED) of Xie and Tu (2015), who showed that an FCN trained to output edge maps instead of class labels is also an excellent edge detector. Their network was initialized

with the VGG object detection network, so arguably the edge detection is supported by the semantic information captured in that network. Variants of HED have been explored by other authors, (Kokkinos, 2016) confirming that CNNs are at present also the state of the art for edge detection.

To undo the loss of spatial resolution due to the pooling layers of FCN, Noh et al. (2015) propose to add an unpooling and upsampling (“deconvolution”) network (Zeiler and Fergus, 2014) on top of it. The result is a sort of encoder-decoder structure that upsamples the segmentation map back to the resolution of the input image. Yang et al. (2016) employ a similar strategy for the opposite purpose: their primary goal is not semantic labeling but rather a “semantically informed” edge detection which accentuates edges that lie on object contours. Also related is the work of Bertasius et al. (2015). They find candidate edge pixels with conventional edge detection, read out the activations at those pixels from the convolution layers of the (frozen) VGG object detection network, and separately train a classifier on the vector of activations to separate object boundaries from other edges. For semantic segmentation, it has also been proposed to additionally add skip connections from lower layers in the encoder part (before pooling) to corresponding decoder layers (after unpooling) so as to re-inject high-frequency image contours into the upsampling process (Dosovitskiy et al., 2015; Marmanis et al., 2016). This architecture has been simplified by the SEGNET model of Badrinarayanan et al. (2017): the fully connected layers are discarded, which drastically reduces the number of free parameters. Moreover, that architecture makes it possible to keep track of pixel indices during max-pooling and restore the values to the correct position during unpooling.

In the context of individual object detection it has been proposed to train the encoder/detector part first, freeze it, and train the decoder part separately (Pinheiro et al., 2016). The DEEPLAB network of Chen et al. (2015) explores a different upsampling strategy: low-resolution output from the FCN is first upsampled bilinearly, then refined with a fully connected CRF (Krähenbühl and Koltun, 2011) whose pairwise potentials are modulated by colour differences in the original image. Later DEEPLAB was extended to simultaneously learn edge detection and semantic segmentation (Chen et al., 2016b). This is perhaps the work most closely related to ours, motivated by the same intuition that there are synergies between the two tasks, because object boundaries often coincide with edges. Going even further, Dai et al. (2016) construct a joint network for detecting object instances, assigning them to a semantic class, and extracting a mask for each

object – i.e., per-object class boundaries. The method is very efficient for well-localized compact objects (“things”), since the object instances can be detected first so as to restrict subsequent processing to those regions of interest. On the other hand, it appears less applicable to remote sensing, where the scene is to a large extent composed of objects without a well-defined bounding box (“stuff”).

Regarding applications in remote sensing, shallow neural networks were already used for semantic segmentation before the advent of deep learning, e.g. [Bischof et al. \(1992\)](#) use a classical multi-layer perceptron to predict the semantic class of a pixel from a small neighborhood window. Shallow architectures are still in use: [Malmgren-Hansen et al. \(2015\)](#) train a relatively shallow CNN with 3 convolution layer and 2 pooling layers to classify pixels in SAR images. [Längkvist et al. \(2016\)](#) make per-pixel predictions with shallow CNNs (where the convolution weights are found by clustering rather than end-to-end training) and smooth the results by averaging over independently generated super-pixels. The mentioned works predict individually for each pixel, on the contrary [Mnih and Hinton \(2010\)](#) have designed a shallow, fully connected network for patch-wise prediction of road pixels. An also relatively shallow FCN with 3 convolution layers and 1 pooling layer is used in ([Saito et al., 2016](#)).

In the last few years, different deep CNN variants have been proposed for semantic segmentation of remote sensing images. [Paisitkriangkrai et al. \(2015\)](#) learn three separate 6-layer CNNs that predict semantic labels for a single pixel from three different neighborhoods. The scores are averaged with those of a conventional random forest classifier trained on per-pixel features, and smoothed with a conditional random field. [Marcu and Leordeanu \(2016\)](#) design a network for patchwise 2-class prediction. It takes as input patches of two different sizes (to represent local and global context), passes them through separate deep convolutional architectures, and combines the results in three deep, fully connected layers to directly output  $16 \times 16$  patches of pairwise labels.

More often, recent works adopt the FCN architecture. Overall, the results indicate that the empirical findings from computer vision largely translate to remote sensing images. Both our own work ([Marmanis et al., 2016](#)) and [Sherrah \(2016\)](#) advocate a two-stream architecture that learns separate convolution layers for the spectral information and the DSM channel, and recommend to start from pretrained networks for the spectral channels. Our work further supports the practice of training multiple copies of the same CNN

architecture and averaging their results ([Marmanis et al., 2016](#)), and [Sherrah \(2016\)](#) reports that the a-trous convolution trick slightly mitigates the information loss due to pooling, at the cost of much larger ( $40\times$ ) computation times. [Mou and Zhu \(2016\)](#) prefer to avoid upsampling altogether, and instead combine the coarser semantic segmentation with a super-pixel segmentation of the input image to restore accurate segmentation boundaries (but not small objects below the scale of the FCN output). Of course, such a strategy cannot be trained end-to-end and heavily depends on the success of the low-level super-pixel segmentation.

A formal comparison between per-pixel CNNs and FCNs has been carried out by [Volpi and Tuia \(2017\)](#). It shows advantages for FCN, but unfortunately both networks do not attain the state of the art, presumably because their encoder-decoder network lacks skip connections to support the upsampling steps, and has been trained from scratch, losing the benefit of large-scale pretraining. A similar comparison is reported in ([Kampffmeyer et al., 2016](#)), with a single upsampling layer, and also trained from scratch. Again the results stay below the state-of-the-art but favor FCN. Median-balancing of class frequencies is also tested, but seems to introduce a bias towards small classes. An interesting aspect of that paper is the quantification of the network’s prediction uncertainty, based on the interpretation of drop-out as approximate Bayesian inference ([Gal and Ghahramani, 2016](#)). As expected, the uncertainty is highest near class-contours.

### 3. The Model

In the following, we describe our network architecture for boundary-aware semantic segmentation in detail. Following our initial hypothesis, we include edge detection early in the process to support the subsequent semantic labeling. As further guiding principles, we stick to the deep learning paradigm and aim for models that can be learned end-to-end; we build on network designs, whose performance has been independently confirmed; and, where possible, we favor efficient, lean networks with comparatively few tunable weights as primary building blocks.

When designing image analysis pipelines there is invariably a trade-off between performance and usability, and DCNNs are no exception. One can get a respectable and useful result with a rather elegant and clean design, or push for maximum performance on the specific task, at the cost of a (often considerably) more complex and unwieldy model. In this work we explore

both directions: on the one hand, our basic model is comparatively simple with  $8.8 \cdot 10^7$  free parameters ( $\text{HED} \cdot \text{H} + \text{SEG} \cdot \text{H}$ , single-scale; see description below), and can be trained with modest amounts of training data. On the other hand, we also explore the maximum performance our approach can achieve. Indeed, our high-end model, with multi-scale processing and ensemble learning, achieves >90% overall accuracy on the ISPRS Vaihingen benchmark. But diminishing returns mean that this requires a more convoluted architecture with 9× higher memory footprint and training time.

Since remote sensing images are too large to pass through a CNN, all described networks operate on tiles of  $256 \times 256$  pixels. We classify overlapping tiles with three different strides (150, 200, and 220 pixels) and sum the results.

We start by introducing the building blocks of our model, and then describe their integration and the associated technical details. Throughout, we refrain from repeating formal mathematical definitions for their own sake. Equation-level details can be found in the original publications. Moreover, we make our networks publicly available to ensure repeatability.<sup>3</sup>

### 3.1. Building blocks

#### SEG·H encoder-decoder network

SEGNET (Badrinarayanan et al., 2017) is a crossbreed between a fully convolutional network (Long et al., 2015) and an encoder-decoder architecture. The input image is first passed through a sequence of convolutions, *ReLU* and *max-pooling* layers. During *max-pooling*, the network tracks the spatial location of the winning maximum value at every output pixel. The output of this *encoding* stage is a representation with reduced spatial resolution. That “bottleneck” forms the input to the *decoding* stage, which has the same layers as the encoder, but in reverse order. Max-pooling layers are replaced by *unpooling*, where the values are restored back to their original location, then convolution layers interpolate the higher-resolution image.

Since the network does not have any fully connected layers (which consume >90% of the parameters in a typical image processing CNN) it is much lighter. SEGNET is thus very memory-efficient and comparatively easy to train. We found, in agreement with its creators, that SEGNET on its own does not always reach the performance of much heavier architectures with

---

<sup>3</sup><https://github.com/deep-unlearn/ISPRS-Classification-With-an-Edge>

fully connected layers. However, it turns out that *in combination with learned class boundaries*, SEGNET matches the more expensive competitors, see Section 4.

Our variant, denotes as SEG·H, consists of two parallel SEGNET branches, one for the colour channels and one for the digital elevation model (DEM). The colour branch is initialized with the existing SEGNET weights, as trained on the Pascal dataset<sup>4</sup> by [Badrinarayanan et al. \(2017\)](#). The second branch processes a two-channel image consisting of nDSM and DSM, and is initialized randomly using "Xavier" weight initialization, a technique designed to keep the gradient magnitude roughly the same across layers ([Glorot and Bengio, 2010](#)). The outputs from the two streams are then concatenated, and fed through a  $1 \times 1$  convolution that linearly combines the vector of feature responses at each location into a score per class. Those class scores are further converted to probabilities with a *softmax* layer.

[Kokkinos \(2016\)](#) reported significant quantitative improvements by an explicit multi-scale architecture, which passes down-scaled versions of the input image through identical copies of the network and fuses the results. Given the small size of SEG·H we have also experimented with that strategy, using three scales. We thus set up three copies of the described two-stream SEG·H with individual per-scale weights. Their final predictions, after fusing the image and height streams, are upsampled as needed with fractional stride convolution layers<sup>5</sup> and fused before the final prediction of the class scores. The multi-scale strategy only slightly improves the results by <0.5%, presumably because remote sensing images, taken in nadir direction from distant viewpoints, exhibit only little perspective effect and thus less scale variation (only due to actual scale variability in metric object coordinates). Still, the small improvement is consistent over all tiles of our validation set, hence we include the multi-scale option in the high-end variant of our system.

#### HED·H *boundary-detection network*

We aim to include explicit boundary information in our processing, thus we require an edge detector that can be integrated into the labeling framework. In a nutshell, HED (Holistically-Nested Edge Detection) is an multi-

---

<sup>4</sup>[http://mi.eng.cam.ac.uk/~agk34/resources/SegNet/segnets\\_pascal.caffemodel](http://mi.eng.cam.ac.uk/~agk34/resources/SegNet/segnets_pascal.caffemodel)

<sup>5</sup>Sometimes inaccurately called "deconvolution" layers. Technically, these layers perform convolution, but sample the input feature maps from the previous layer with a stride <1. E.g., a stride of  $\frac{1}{2}$  will double the resolution.

scale encoder-decoder CNN trained to output an image of edge likelihoods. An important feature of HED is that it uses multi-scale prediction in conjunction with deep supervision (Lee et al., 2015). That is, the (rectified) output of the last convolution before each pooling layer is read out of the network as prediction for that particular scale, and supervised during training by an additional (Euclidean distance) loss function. The multi-scale predictions are then combined into a final boundary probability map. Importantly, even though HED has no explicit mechanism to enforce closed contours, we find that by learning from global image context it does tend to generate closed contours, which is important to support our segmentation task.

For our purposes, we again add a second branch for the DSM, and modify HED to better take into account the uncertainty of boundary annotations, by using a regression loss w.r.t. a continuous “boundary score”  $\mathbf{y}$  rather than a hard classification loss. The intuition is that the location of a class boundary has an inherent uncertainty. We therefore prefer to embrace and model the uncertainty, and predict the “likelihood” of the boundary being present at a certain pixel. The advantage is best explained by looking at pixels very close to the annotated boundary: using those pixels as negative (i.e., background) training samples will generate label noise; using them as positive samples contradicts the aim to predict precise boundary locations; and excluding them from the training altogether means depriving the network of training samples close to the boundary, where they matter most. For our task, the desired edges are the segment boundaries, i.e., the label transitions in the training data. To turn them into soft scores we dilate the binary boundary image with a diamond structuring element. The structuring element defines the width of the “uncertainty band” around an annotated boundary and depends on the ground sampling distance.

Then, we weight each class-boundary pixel according to its truncated Euclidean distance to the nearest background pixel, using the distance transform:  $Y = \beta \cdot D_t^{\ell 2}(B_d)$ . The operator  $D_t^{\ell 2}(B_d)$  denotes the truncated Euclidean distance from a particular pixel to the nearest background pixel. The factor  $\beta = \frac{|B_d=0|}{|B_d|}$  compensates the relative frequencies of boundary and background pixels, to avoid overfitting to the dominant background. Finally, the weights are normalized to the interval  $[0 \dots 1]$  to be consistent with the original HED model. As above, we set up two separate streams for color images and for the height also during boundary detection, and refer to our version as HED·H. The image stream is initialized with the original HED weights, whereas the DEM stream is trained from scratch. For output (including

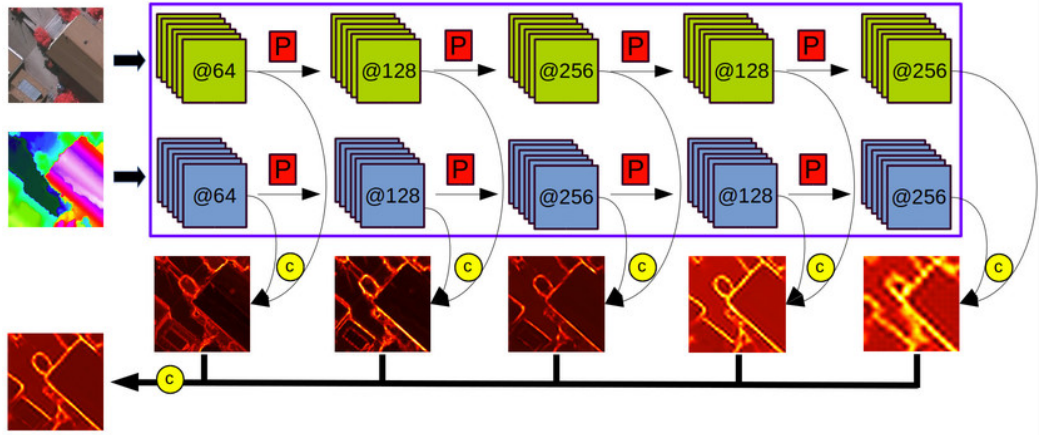


Figure 2: The Class-Boundary network  $\text{HED}\cdot\text{H}$ . Color and height are processed in separate streams. Before each pooling level (red squares) the network outputs a set of scale-dependent class-boundaries, which are fused into the final multi-scale boundary prediction. Yellow circles denote concatenation of feature maps.

side outputs) the two streams are fused by concatenation, convolution with a  $1 \times 1$  kernel and fractional convolution to the output resolution. A graphical overview of the boundary network is given in Figure 2, visual results of class-boundaries are shown in Figure 3.

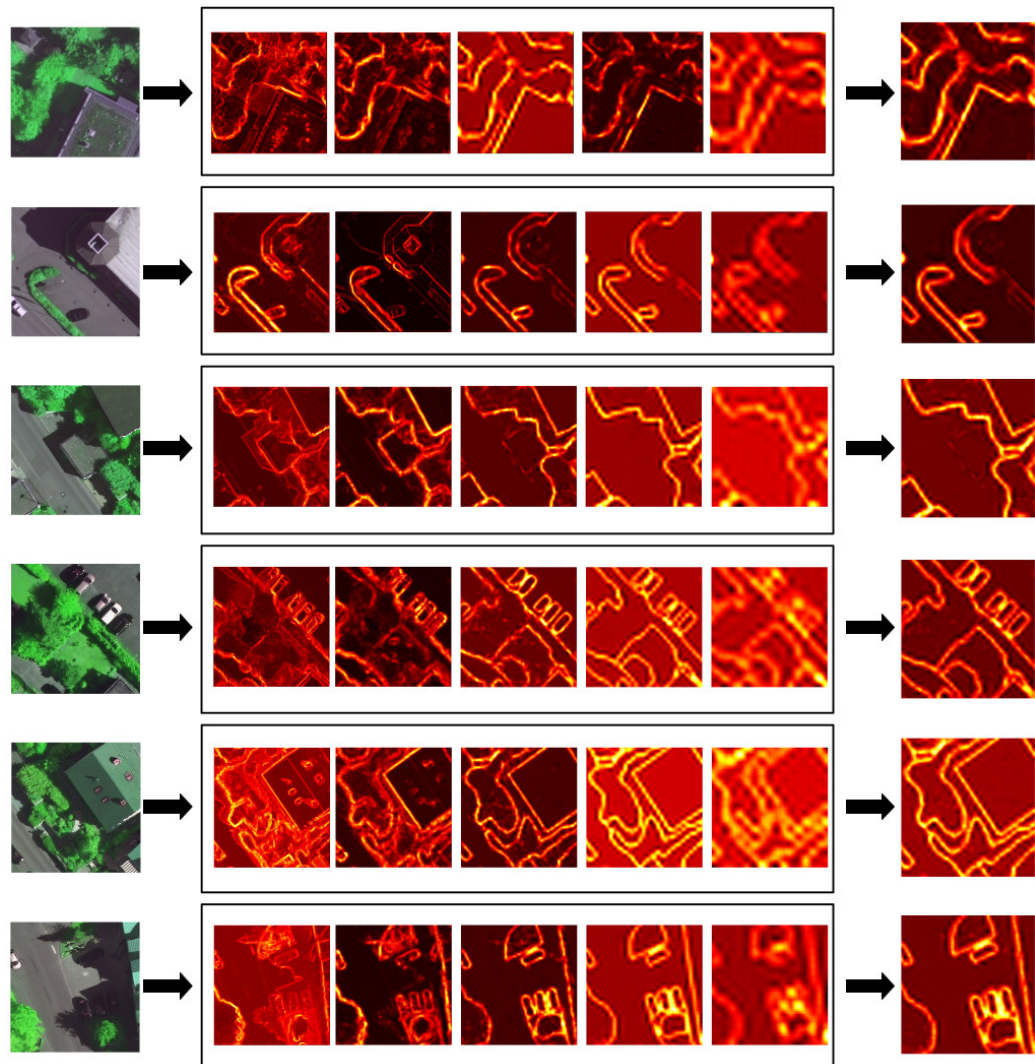


Figure 3: Examples of class boundary predictions. Left: input image. Middle: per-scale outputs. Right: estimated multi-scale boundary map.

### *FCN·H semantic segmentation network*

From the literature ([Simonyan and Zisserman, 2014](#)) it is known that, also for strong classifiers like CNNs, ensemble averaging tends to improve classification results. We thus also experiment with an ensemble of multiple CNNs. To that end we use our previous semantic segmentation network, here termed FCN·H, which has already shown competitive performance for remote sensing problems ([Marmanis et al., 2016](#)). That model in fact is an ensemble of two identical FCN architectures initialized with different weights, namely those of *VGG* and *Pascal*, see [Marmanis et al. \(2016\)](#). For clarity we refer to the ensemble as FCN·H, and to its two members as FCN·H-V, respectively FCN·H-P. Contrary to SEG·H this model is derived from the standard FCN and has fully connected layers. It is thus heavier in terms of memory and training, but empirically improves the predictions, presumably because the network can learn extensive high-level, global object information. Compared to the original FCN ([Long et al., 2015](#)), our variant has additional skip connections to minimize information loss from downsampling. As above, it has separate streams for image and DEM data.

### *3.2. Integrated class boundary detection and segmentation*

Our strategy to combine class boundary detection with semantic segmentation is straight-forward: we append the class-boundary network (HED·H) before the segmentation network (FCN·H or SEG·H) and train the complete architecture. In the image stream, the input is the raw colour image; in the DSM stream it is a 2-channel image consisting of the raw DSM and the nDSM (generated by automatically filtering above-ground objects and subtracting the result from the DSM). In both cases, the input is first passed through the HED·H network (Figure 4(top)), producing a scalar image of boundary likelihoods. That image is concatenated to the raw input as an additional channel to form the input for the corresponding stream of the semantic segmentation network (note, in CNN language this can be seen as a skip connection that bypasses the boundary detection layers). For SEG·H, a further skip connection bypasses most of the segmentation network and reinjects the colour image boundaries as an extra channel after merging the image and DSM streams, see Figure 4(middle). This additional skip connection re-introduces the class-boundaries deep into the classifier, immediately before the final label prediction. For FCN·H this did not seem necessary, since the architecture already includes a number of long skip connections from rather early layers, see Figure 4(bottom). The entire processing chain is trained end-to-end (see

below for details), using boundaries as supervision signal for the HED·H layers and segmentations for the remaining network.

### 3.3. Ensemble learning

As discussed above, ensemble averaging typically improves DCNN predictions further. We thus also test that strategy and combine the predictions of three different boundary-aware networks (given the effort to train deep networks, “ensembles” are typically small). As described above, we have trained two versions of the FCN·H network with integrated HED·H boundary detector, one initialized with the original FCN (Pascal VOC) weights<sup>6</sup> and the other initialized with weights from the VGG-16 variant.<sup>7</sup> Their individual performance is comparable, with FCN·H-V slightly better overall. In both cases, the DEM channel is again trained from random initializations.

Ensemble predictions are made by simply averaging the individual class probabilities predicted by FCN·H-V, FCN·H-P and SEG·H.<sup>8</sup> Empirically the ensemble predictions give a significant performance boost, seemingly FCN·H and SEG·H are to some degree complementary, see experimental results in Section 4. Note though, the two FCN·H models, each with >100 million parameters (see section 4), are memory-hungry and expensive to train, thus we do not generally recommend such a procedure, except when aiming for highest accuracy. Figure 5 depicts the complete ensemble.

---

<sup>6</sup><http://dl.caffe.berkeleyvision.org/fcn32s-heavy-pascal.caffemodel>

<sup>7</sup>[http://www.robots.ox.ac.uk/~vgg/software/very\\_deep/caffe/VGG\\_ILSVRC\\_16\\_layerscaffemodel](http://www.robots.ox.ac.uk/~vgg/software/very_deep/caffe/VGG_ILSVRC_16_layerscaffemodel)

<sup>8</sup>We did not experiment with trained fusion layers, since the complete ensemble is too large to fit into GPU memory.

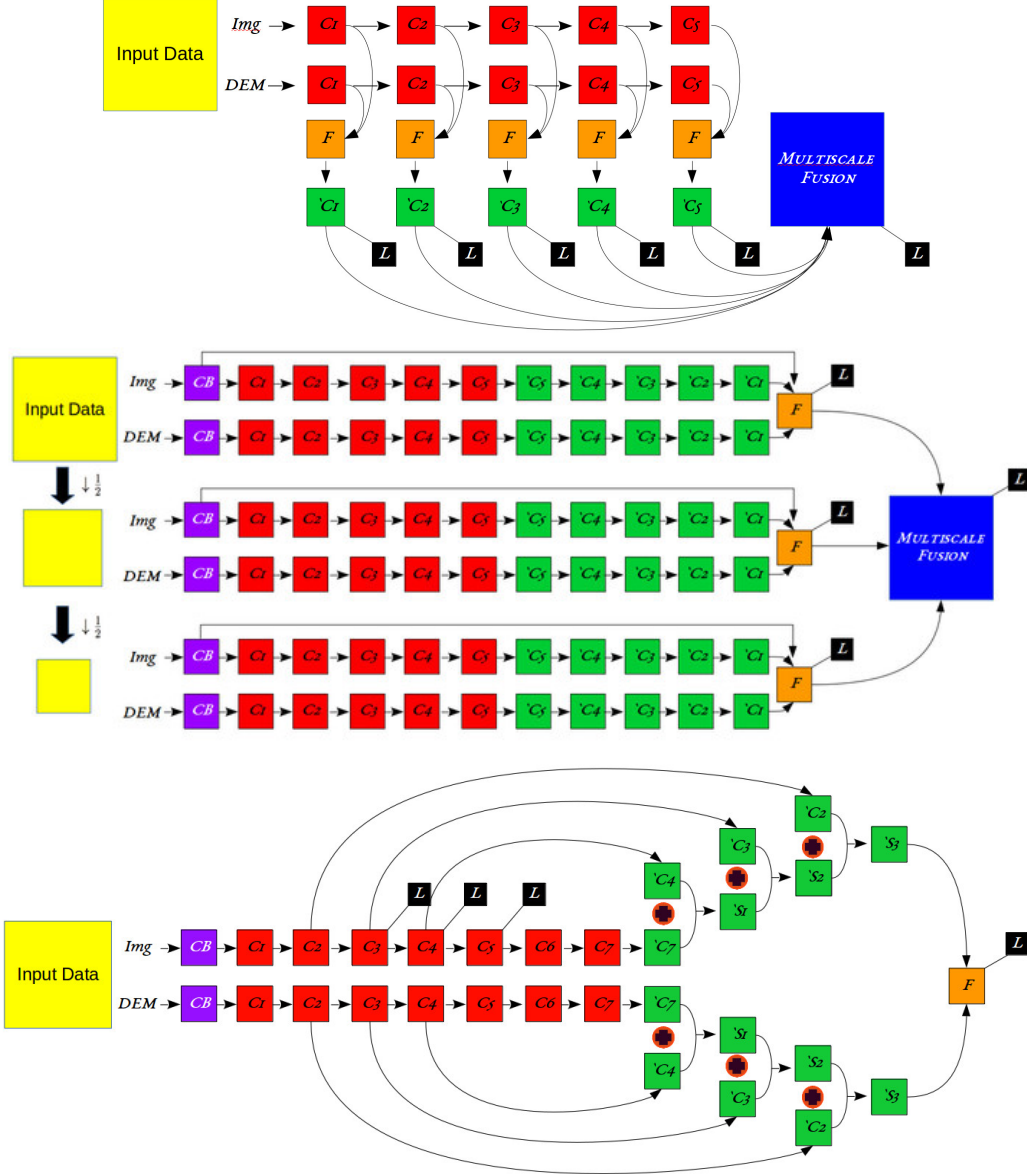


Figure 4: CNN architectures tested in this work. Top: HED-H architecture for class-boundary delineation. Middle: multi-scale SEG-H architecture. Bottom: FCN-H-P architecture (identical to FCN-H-V except for initial weights). The boundary detection network is collapsed (violet box) for better readability. Encoder parts that reduce spatial resolution are marked in red, decoder parts that increase resolution are green. Orange denotes fusion by concatenation,  $(1 \times 1)$  convolution, and upsampling (as required). The red circle with the plus sign denotes element-wise summation of feature maps, the black box symbolises the (logistic, respectively Euclidean) loss.

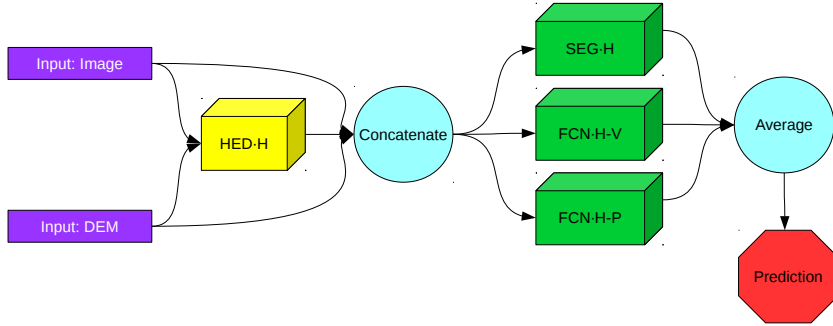


Figure 5: Ensemble prediction with  $\text{SEG}\cdot\text{H}$ ,  $\text{FCN}\cdot\text{H}\text{-P}$  and  $\text{FCN}\cdot\text{H}\text{-V}$ . The  $\text{HED}\cdot\text{H}$  component extracts the class boundaries.

### 3.4. Implementation details and training

The overall network with boundary detection is fairly deep, and the boundary and labeling parts use different target outputs and loss functions. We found that under these circumstances training must proceed in stages to achieve satisfactory performance, even if using pre-trained components. A cautious strategy, in which each component is first trained separately, gave the best results. First, we train the boundary detector ( $\text{HED}\cdot\text{H}$ ) separately, using  $\text{HED}$  weights to initialize the image stream and small random weights for the DSM stream. That step yields a DCNN boundary detector tailored to our aerial data. The actual segmentation network and loss is added only after this strong “initialization” of the boundary detector. Thus, the boundary detector from the start delivers sensible results for training the semantic labeling component, and only needs to be fine-tuned to optimally interact with the subsequent layers. Moreover, for  $\text{SEG}\cdot\text{H}$  that two-stage training is carried out separately for each of the three scales. The separate single-scale segmentation networks are then combined into one multi-scale architecture and refined together. Empirically, separating the scales stabilizes the learning of the lower resolutions. When trained together immediately, they tend to converge to weak solutions and the overall result is dominated by the (still very competitive) highest resolution.

*Normalization of gradients.* Regarding the common problem of exploding or vanishing gradients during training, we stuck to the architectures recommended by the original authors, meaning that  $\text{SEG}\cdot\text{H}$  does use *batch normalization* (Badrinarayanan et al., 2017), while  $\text{HED}\cdot\text{H}$  does not (Xie and Tu,

2015). A pragmatic solution is to use a large base learning rate appropriate for SEG-H and add layer-specific scale factors to decrease the learning rate in the HED-H layers. We also found that batch normalization in the final layers, after the SEG-H decoder phase, strongly sparsifies the feature maps. For our goal of dense per-pixel prediction this effect is detrimental, causing a  $\approx 1\%$  drop in labeling accuracy. We thus switch-off batch normalization for those layers.

*Drop-out.* The original SEGNET relies heavily on drop-out. The authors recommend to randomly drop 50% of the trainable decoder weights in each iteration. We found this drastic regularization to negatively affect our results, thus we decrease it to 20% for the highest resolution, respectively 10% for the two lower ones. Further research is needed to understand this big difference. We suspect that it might have to do with the different image statistics. In close-range images, each object normally covers a large image area, thus both image intensities and semantic labels are strongly correlated over fairly large regions. In remote sensing data, with its many small objects, nearby activations might not be able to “stand in” as easily for a dropped connection, especially in the early layers of the decoder.

*Data Augmentation.* DCNNs need large amounts of training data, which are not always available. It is standard practice to artificially increase the amount and variation of training data by randomly applying plausible transformations to the inputs. Synthetic data augmentation is particularly relevant for remote sensing data to avoid over-fitting: in a typical mapping project the training data comes in the form of a few spatially contiguous regions that have been annotated, not as individual pixels randomly scattered across the region of interest. This means that the network is prone to learn local biases like the size of houses or the orientation of the road network particular to the training region. Random transformations – in the example, scaling and rotation – will mitigate such over-fitting.

In our experiments we used the following transformations for data augmentation, randomly sampled per mini-batch of the stochastic gradient descent (SGD) optimisation: scaling in the range [1 … 1.2], rotation by  $[0^\circ \dots 15^\circ]$  degrees, linear shear with  $[0^\circ \dots 8^\circ]$ , translation by  $[-5 \dots 5]$  pixels, and reflections w.r.t. the vertical and horizontal axis (independently, with equal probability).



Figure 6: Annotation ambiguity of trees in leaf-off condition in the Potsdam dataset. Even though there is no image evidence (left), annotators tend to hallucinate a tree crown around the empty branches, denoted by yellow color in the labels (middle). The corresponding label class-boundaries (right) do not reflect discontinuities in the input images, thus contradicting our model assumptions.

## 4. Experiment Results

### 4.1. Datasets

#### *ISPRS Vaihingen Dataset*

We conduct experimental evaluations on the ISPRS Vaihingen 2D semantic labeling challenge. This is an open benchmark dataset provided online.<sup>9</sup> The dataset consists of a color infrared orthophoto, a DSM generated by dense image matching, and manually annotated ground truth labels. Additionally, a nDSM has been released by one of the organizers (Gerke, 2014), generated by automatically filtering the DSM to a DTM and subtracting the two. Overall, there are 33 tiles of  $\approx 2500 \times 2000$  pixels at a GSD of  $\approx 9\text{cm}$ . 16 tiles are available for training and validation, the remaining 17 are withheld by the challenge organizers for testing. We thus remove 4 tiles (image numbers 5, 7, 23, 30) from the training data and use them as validation set for our experiments. All results refer to that validation set, unless noted otherwise.

#### *ISPRS Potsdam Dataset*

We additionally conduct experiments on the ISPRS Potsdam semantic labeling dataset.<sup>10</sup> The data is rather similar to Vaihingen, with 4-band

---

<sup>9</sup><http://www2.isprs.org/commissions/comm3/wg4/2d-sem-label-vaihingen.html>

<sup>10</sup><http://www2.isprs.org/commissions/comm3/wg4/2d-sem-label-potsdam.html>

RGB-IR images, as well as DSM and nDSM from dense matching and filtering. There are 38 image tiles of size  $6000 \times 6000$  pixels, with GSD  $\approx 5\text{cm}$ . 24 tiles are densely annotated for training, whereas the remaining 14 are withheld as test set. For our experiments we have removed four tiles (image numbers 7\_8, 4\_10, 2\_11, 5\_11) from the training data and use them as validation set. All statistics on Potsdam refer to that validation set.

We point out an issue with the reference data of Potsdam, which has implications for our method: the trees are mostly deciduous and the data was recorded in leaf-off conditions. However, the human annotators appear to have guessed the area of the tree crown from the branches and have drawn an imaginary, solid crown area. This annotation contradicts the image evidence, see Figure 6. In particular, semantic boundaries extracted from the reference data are not aligned with actual image discontinuities. We also note that, other than in Vaihingen, there are comparatively large areas marked as *background* (rejection) class, with large intra-class variability.

#### *Training details and parameters*

As described above, each labeling and boundary detection network was first trained individually to convergence, then the pretrained pieces were assembled and fine-tuned by further training iterations. For a tally of the unknown weights, see Table 1.

For the individual network parts, we always start from a quite high learning rate ( $lr=10^{-8}$ ) and decrease it by a factor  $\times 10$  every 12000 iterations. The total of number of iterations was 100000. The SEG-H part was trained with batch size 2, the HED-H boundary detector with batch size 5.

The complete, assembled boundary+segmentation model was trained for 30000 iterations, starting with a smaller learning rate ( $lr=10^{-12}$ ). Batch size had to be reduced to 1 to stay within the memory capacity of an Nvidia Titan-X GPU.

The remaining hyper-parameters were set to  $momentum = 0.9$  and  $weight-decay = 0.00015$ , for all models.

#### *4.2. Results*

We evaluate the different components of our model by gradually adding components. We start from the basic SEG-H, augment it with class boundaries, then with multi-scale processing. Finally, we include it in a DCNN ensemble. We will not separately discuss post-processing of the outputs

Table 1: Sizes of model components in terms of trainable parameters. All models are dimensioned to fit on a single Nvidia Titan-X GPU (except for the ensemble, for which averaging is done on the CPU). Suffix *sc1* denotes a single-scale model using only the full resolution, *Msc* denotes the multi-scale model.

|                         |                  |
|-------------------------|------------------|
| HED·H+SEG·H- <i>sc1</i> | $88 \cdot 10^6$  |
| HED·H+SEG·H- <i>Msc</i> | $206 \cdot 10^6$ |
| HED·H+FCN·H-P           | $300 \cdot 10^6$ |
| HED·H+FCN·H-V           | $300 \cdot 10^6$ |
| HED·H+FCN·H+SEG·H       | $806 \cdot 10^6$ |

with explicit smoothness or context models like CRFs. In our tests, post-processing with a fully connected CRF, as for example in (Chen et al., 2016a; Marmanis et al., 2016), did not improve the results – if anything, it degraded the performance on small objects, especially the *car* class. For completeness, results of our networks with and without smoothing are available on the Vaihingen benchmark site. We conclude that our DCNNs already capture the context in large context windows. Indeed, this is in our view a main reason for their excellent performance.

### Basic CNN Results

**Vaihingen:** The basic single-scale SEG·H reaches 84.8% overall accuracy over the validation set. This is in line with other researchers’ findings on the Vaihingen benchmark: straight-forward adaptations of state-of-the-art DCNN models from the computer vision literature typically reach around 85%. Our network performs particularly well on impervious ground and buildings, whereas it is challenged by low vegetation, which is frequently confused with the tree class. Detailed per-class results are given in Table 2.

For comparison, we also run our earlier FCN·H model Marmanis et al. (2016), i.e., an ensemble of only FCN·H-V and FCN·H-P, without explicit class-boundary detection. That model performs comparably, with 85.5% overall accuracy. Interestingly, it is significantly better at classifying low vegetation, and also beats SEG·H on impervious surfaces and trees. On the contrary, it delivers clearly worse segmentations of buildings.

**Potsdam:** On the Potsdam dataset the SEG·H-*sc1* network performs significantly better than the standard FCN·H-P and FCN·H-V, with 84.9%, 80.9% and 81.4%, overall accuracy respectively. The reason for the relatively weak results of the two larger networks is unclear, but we did not manage to im-

prove them further. We will see below that including boundary information closes the performance gap. For detailed results refer to Table 2.

### *Effect of Class Boundaries*

**Vaihingen:** We now go on to evaluate the main claim of our paper, that explicit class boundary detection within the network improves segmentation performance. Adding the HED·H boundary detector to SEG·H reaches 89.8% overall accuracy (HED·H+SEG·H-*sc1*), a gain of more than 5 percent points, see Table 2.

The per-class results in Table 2 reveal that class boundaries significantly boost the performance of SEG·H for *all* target classes, including the vegetation classes that do not have sharp, unambiguous boundaries. We suspect that in vegetation areas, where matching-based DSMs are particularly inaccurate, even imprecise boundaries can play a noticeable role in delimiting high from low vegetation. Moreover, one might speculate that boundaries derived from semantic segmentation maps carry information about the extent and discontinuities at object level, and can to some degree mitigate a main limitation of SEG·H, namely the lack of fully connected layers that could extract long-range context. It is however an open, and rather far-reaching, question to what extent locally derived object boundary information can substitute large-scale semantic context.

For the FCN·H ensemble, we observe a similar, albeit weaker effect. Overall accuracy increases by 3 percent points to 88.8% (HED·H+FCN·H). There are however losses for the *car* and *low vegetation* classes, whereas the gains are due to better segmentation of buildings and trees.

As a side note, we found that the accuracy of the ground truth is noticeably lower for the vegetation classes as well as the cars. This can in part be explained by inherent definition uncertainty, especially in the case of vegetation. Still, we claim that the upper performance bound for automatic segmentation methods is probably well below 100% for Vaihingen, due to uncertainty and biases of the ground truth of both the training and test set. See also Section 4.4.

**Potsdam:** Similar effects can be observed on the Potsdam dataset, where the class boundaries also significantly improve the overall accuracy by up to 4.5 percent points. Detailed results are given in Table 2. An exception from this trend is the tree class in SEG·H-*sc1*: adding class boundaries reduces its correctness significantly, from 74.4% to 68.6%. We attribute this to the guessed tree-crown annotations mentioned above. Since their imagi-

nary boundaries are not reflected in the image data, adding them apparently hurts, rather than helps the localization of the tree outlines. Curiously, the trees do get a boost from boundary information when using the FCN·H-P or FCN·H-V networks. We were not yet able to determine the reason for this behavior. We speculate that possibly these networks, with their higher capacity and pre-training for object detection, can extract additional evidence for the presence/absence of a tree from the edge maps and are better able to infer the “guessed” tree outline from context.

Table 2: Adding an explicit class-boundary model improves semantic segmentation, for both tested CNN architectures and both investigated datasets. HED·H and *sc1* denote use of class-boundaries and restriction to a single scale, respectively. Scores are (true positive) detection rates. See text for details.

|           |                         | <i>Impervious</i> | <i>Building</i> | <i>Low Veg.</i> | <i>Tree</i> | <i>Car</i> | <i>OA</i>     |
|-----------|-------------------------|-------------------|-----------------|-----------------|-------------|------------|---------------|
| Vaihingen | SEG·H- <i>sc1</i>       | 87.5 %            | 93.8 %          | 59.0 %          | 79.0 %      | 63.0 %     | 84.8 %        |
|           | HED·H+SEG·H- <i>sc1</i> | 91.2 %            | 95.6 %          | 70.8 %          | 92.3 %      | 69.0 %     | <b>89.8 %</b> |
|           | FCN·H                   | 89.3 %            | 87.5 %          | 77.3 %          | 88.8 %      | 68.3 %     | 85.8 %        |
|           | HED·H+FCN·H             | 89.3 %            | 93.5 %          | 73.0 %          | 90.8 %      | 62.0 %     | 88.8 %        |
| Potsdam   | SEG·H- <i>sc1</i>       | 84.7 %            | 95.2 %          | 78.9 %          | 74.4 %      | 80.8 %     | 84.9 %        |
|           | HED·H+SEG·H- <i>sc1</i> | 85.0 %            | 96.7 %          | 84.2 %          | 68.6 %      | 85.8 %     | <b>85.1 %</b> |
|           | FCN·H-P                 | 84.0 %            | 88.5 %          | 72.0 %          | 74.7 %      | 75.0 %     | 80.9 %        |
|           | HED·H+FCN·H-P           | 84.9 %            | 96.2 %          | 76.7 %          | 79.1 %      | 86.7 %     | 84.5 %        |
|           | FCN·H-V                 | 84.3 %            | 90.6 %          | 71.8 %          | 74.9 %      | 74.4 %     | 81.4 %        |
|           | HED·H+FCN·H-V           | 85.2 %            | 96.8 %          | 74.3 %          | 79.1 %      | 85.4 %     | 85.0 %        |

### *Effect of Multi-scale CNN*

**Vaihingen:** Next, we test what can be gained by explicit multi-scale processing. This is inspired by Kokkinos (2016), who show significant improvements with multi-scale processing. Our implementation uses exactly the same architecture, with three streams that independently process inputs of different scale and fuse the results within the network.

We run this option only for SEG·H. The FCN·H network has multiple fully connected layers and should therefore be able to capture context globally over the entire input region, thus we do not expect an explicit multi-scale version to improve the results. Moreover, it is too large to fit multiple copies of the network into GPU memory.

Empirically, multi-scale processing did not improve the results to the same extent as in (Kokkinos, 2016). We only gain 0.2 percent points, see

**Table 3.** Apparently, the single-scale network already captures the relevant information. We suspect that the gains from an explicit multi-scale architecture are largely achieved by better covering strong scale variations due to different perspective effects and camera viewpoints. In nadir-looking remote sensing images such effects are absent and scale variations occur only due to actual size variations in object space, which seem to be adequately captured by the simpler network. Nevertheless, since the gains are quite consistent across different validation images, we keep the multi-scale option included for the remaining tests on Vaihingen. We note though, this triples the memory consumption and is therefore not generally recommended. Given the small differences, we did not employ multi-scale processing in the Potsdam experiments.

Table 3: Multi-scale processing and ensemble learning over the ISPRS Vaihingen dataset. The results (overall accuracies) on the validation set confirm that gains are mostly due to the class boundary detection, whereas multi-scale processing and ensemble prediction only slightly improve the results further. See text for details.

|           | <i>Scene</i>    | HED·H+FCN·H+SEG·H | HED·H+SEG·H- <i>Msc</i> | HED·H+SEG·H- <i>sc1</i> | SEG·H- <i>sc1</i> | HED·H+FCN·H | FCN·H  |
|-----------|-----------------|-------------------|-------------------------|-------------------------|-------------------|-------------|--------|
| Vaihingen | <i>Image 5</i>  | 91.5 %            | 91.2 %                  | 91.1 %                  | 86.2 %            | 90.4 %      | 86.3 % |
|           | <i>Image 7</i>  | 89.2 %            | 89.6 %                  | 89.6 %                  | 84.2 %            | 89.1 %      | 87.1 % |
|           | <i>Image 23</i> | 92.0 %            | 90.8 %                  | 90.2 %                  | 85.6 %            | 89.3 %      | 83.7 % |
|           | <i>Image 30</i> | 88.7 %            | 88.5 %                  | 88.4 %                  | 83.2 %            | 86.7 %      | 86.1 % |
|           | <i>OA</i>       | <b>90.3 %</b>     | 90.0 %                  | 89.8 %                  | 84.8 %            | 88.8 %      | 85.8 % |

Table 4: Results on Potsdam validation set for individual networks and network ensemble. The class boundaries improve the classification accuracy of all three individual networks, and thus also of the ensemble.

|         | <i>Scene</i>      | HED·H+FCN·H+SEG·H | HED·H+SEG·H- <i>sc1</i> | SEG·H- <i>sc1</i> | HED·H+FCN·H-P | FCN·H-P | HED·H+FCN·H-V | FCN·H-V |
|---------|-------------------|-------------------|-------------------------|-------------------|---------------|---------|---------------|---------|
| Potsdam | <i>Image 2_11</i> | 84.5 %            | 81.1 %                  | 81.9 %            | 82.2 %        | 76.2 %  | 82.9 %        | 78.8 %  |
|         | <i>Image 5_11</i> | 90.9 %            | 89.8 %                  | 89.3 %            | 90.2 %        | 86.2 %  | 90.6 %        | 86.7 %  |
|         | <i>Image 4_10</i> | 81.8 %            | 83.3 %                  | 82.7 %            | 79.2 %        | 79.2 %  | 79.6 %        | 79.2 %  |
|         | <i>Image 7_8</i>  | 87.7 %            | 86.3 %                  | 85.6 %            | 86.6 %        | 81.6 %  | 86.7 %        | 80.9 %  |
|         | <i>OA</i>         | <b>86.2 %</b>     | 85.1 %                  | 84.9 %            | 84.5 %        | 80.9 %  | 85.0 %        | 81.4 %  |

### *Effect of the Ensemble*

**Vaihingen:** Several works have confirmed that also for DCNN models ensemble learning is beneficial to reduce individual model biases. We have

also observed this effect in earlier work and thus test what can be gained by combining several *boundary-aware* segmentation networks.

We run the three introduced networks  $\text{SEG}\cdot\text{H}$ ,  $\text{FCN}\cdot\text{H}\text{-P}$  and  $\text{FCN}\cdot\text{H}\text{-V}$ , all with an integrated  $\text{HED}\cdot\text{H}$  boundary detector, and average their predictions. The ensemble beats both the stand-alone  $\text{SEG}\cdot\text{H}$  model and the two-model ensemble of (boundary-enhanced)  $\text{FCN}\cdot\text{H}$ , see Table 3. The advantage over  $\text{SEG}\cdot\text{H}$  is marginal, whereas a clear improvement can be observed over  $\text{FCN}\cdot\text{H}$ . In other words,  $\text{SEG}\cdot\text{H}$  alone stays behind its  $\text{FCN}\cdot\text{H}\text{-V}$  and  $\text{FCN}\cdot\text{H}\text{-P}$  counterparts, but when augmented with class-boundaries it outperforms them, and reaches almost the performance of the full ensemble. It seems that for the lighter and less global  $\text{SEG}\cdot\text{H}$  model the boundary information is particularly helpful.

We point out that, by and large, the quantitative behavior is consistent across the four individual tiles of the validation set. In all four cases,  $\text{HED}\cdot\text{H}+\text{FCN}\cdot\text{H}$  clearly beats  $\text{FCN}\cdot\text{H}$ , and similarly  $\text{HED}\cdot\text{H}+\text{SEG}\cdot\text{H}\text{-sc1}$  comprehensively beats  $\text{SEG}\cdot\text{H}\text{-sc1}$ . Regarding multi-scale processing,  $\text{HED}\cdot\text{H}+\text{SEG}\cdot\text{H}\text{-Msc}$  wins over  $\text{HED}\cdot\text{H}+\text{SEG}\cdot\text{H}\text{-sc1}$  except for one case (image 7), where the difference are a barely noticeable 0.03 percent points (ca. 1500 pixels / 12 m<sup>2</sup>). Ensemble averaging again helps for the other three test tiles, with an average gain of 0.21 percent points, while for image 7 the ensemble prediction is better than  $\text{HED}\cdot\text{H}+\text{FCN}\cdot\text{H}$  but does not quite reach the  $\text{SEG}\cdot\text{H}$  performance. A further analysis of the results is left for future work, but will likely require a larger test set. For a visual impression, see Figure 7.

**Potsdam:** For the ensemble model we proceed in the same way and average the individual predictions of  $\text{SEG}\cdot\text{H}$ ,  $\text{FCN}\cdot\text{H}\text{-P}$  and  $\text{FCN}\cdot\text{H}\text{-V}$ . Also for Potsdam, the ensemble with class boundary support for each of the three members performs best, see Table 4. Note that, although all three networks exhibit almost identical overall performance of 85%, averaging them boosts the accuracy by another percent point. Visual examples are shown in Figure 8.

#### *Effects of nDSM Errors*

**Vaihingen:** On the official Vaihingen test set the performance of our ensemble drops to 89.4%, see below. We have visually checked the results and found a number of regions with large, uncharacteristic prediction errors. It turns out that there are gross errors in the test set that pose an additional, presumably unintended, difficulty. In the nDSM of Gerke (2014), a number of large industrial buildings are missing, since the “ground” surface follows

their roofs, most likely due to incorrect filtering parameters. The affected buildings cover a significant area: 3.1% (154'752 pixels) of image 12, 9.3% (471'686 pixels) of image 31, and 10.0% (403'818 pixels) of image 33.

By itself this systematic error could be regarded as a recurring deficiency of automatically found nDSMs, which should be handled by the semantic segmentation. But unfortunately, they only occur in the test set, while in the training set no comparable situations exist. It is thus impossible for a machine learning model to handle them correctly.

To get an unbiased result we thus manually corrected the nDTMs of the four affected buildings. We then reran the testing, without altering the trained model in any way, and obtained an overall accuracy of 90.3%, almost perfectly in line with the one on our validation set, and 0.9 percent points up from the biased result.

In the following evaluation we thus quote both numbers. We regard the 90.3% as our “true” performance on a test set whose properties are adequately represented in the training data. Since competing methods did however, to our knowledge, not use the corrected test set, they should be compared to the 89.4% achieved with the biased nDSM. We note however that the discovered errors are significant in the context of the benchmark: the bias of almost 1 percent point is larger than the typical differences between recent competing methods. Since the experiment mainly serves to illustrate the quality and influence of the available reference data, we did not repeat it for Potsdam (where it would have been very hard to repair especially the tree annotations).

#### 4.3. Comparison to state of the art

**Vaihingen:** Our proposed *class-contour ensemble model* is among the top performers on the official benchmark test set, reaching 89.4% overall accuracy, respectively 90.3% with the correct nDSM. Note, the model names on the benchmark website differ from those used here, please refer to Table 6. The strongest competitors at the time of writing<sup>11</sup> were INRIA (89.5%, [Maggiori et al., 2016](#)), using a variant of FCN, and ONERA (89.8%, [Audebert et al., 2016](#)), with a variant of SEGNET. Importantly, we achieve above 90%

---

<sup>11</sup>The field moves forward at an astonishing pace, during the review of the present paper several groups have reached similar or even slightly higher accuracy. We cannot comment on these works, since no descriptions of their methodologies have appeared yet.

accuracy over man-made classes, which are the most well-defined ones, where accurate segmentation boundaries matter most, see Table 5.

Detailed results for the top-ranking published models in the benchmark are given in Table 7. Table 6 lists the benchmark identifiers of the different model variants we have described. Overall, the performance of different models is very similar, which may not be all that surprising, since the top performers are in fact all variants of FCN or SEGNET. We note that our model and INRIA are the most “puristic” ones, in that they do not use any hand-engineered image features. ONERA uses the NDVI as additional input channel; DST seemingly includes a random forest in its ensemble, whose input features include the NDVI (Normalized Vegetation Index) as well as statistics over the DSM normals. It appears that the additional features enable a similar performance boost as our class boundaries, although it is at this point unclear whether they encode the same information. Interestingly, our model scores rather well on the *car* class, although we do not use any stratified sampling to boost rare classes. We believe that this is in part a consequence of not smoothing the label probabilities.

One can also see that after correcting the nDSM for large errors, our performance is better than most competitors on impervious surfaces as well as on buildings. The bias in the test data thus seems to affect all models. Somewhat surprisingly, our scores on the vegetation classes are also on par with the competitors, although intuitively contours cannot contribute as much for those classes, because their boundaries are not well-defined. Still, they significantly improve the segmentation of vegetation, c.f. Table 2. Empirically, the class-boundary information boosts segmentation of the *tree* and *low vegetation* classes to a level reached by models that use a dedicated NDVI channel. A closer look at the underlying mechanisms is left for future work.

#### 4.4. A word on data quality

In our experiments, we repeatedly noticed inaccuracies of the ground truth data, such as those shown in Figure 9 (similar observations were made by Paisitkriangkrai et al. (2015)). Obviously, a certain degree of uncertainty is unavoidable when annotating data, in particular in remote sensing images with their small objects and many boundaries. We thus decided to re-annotate one image (*image-23*) from our Vaihingen validation set with great care, to assess the “inherent” labeling accuracy. We did this only for the two easiest classes *buildings* and *cars*, since the remaining classes have

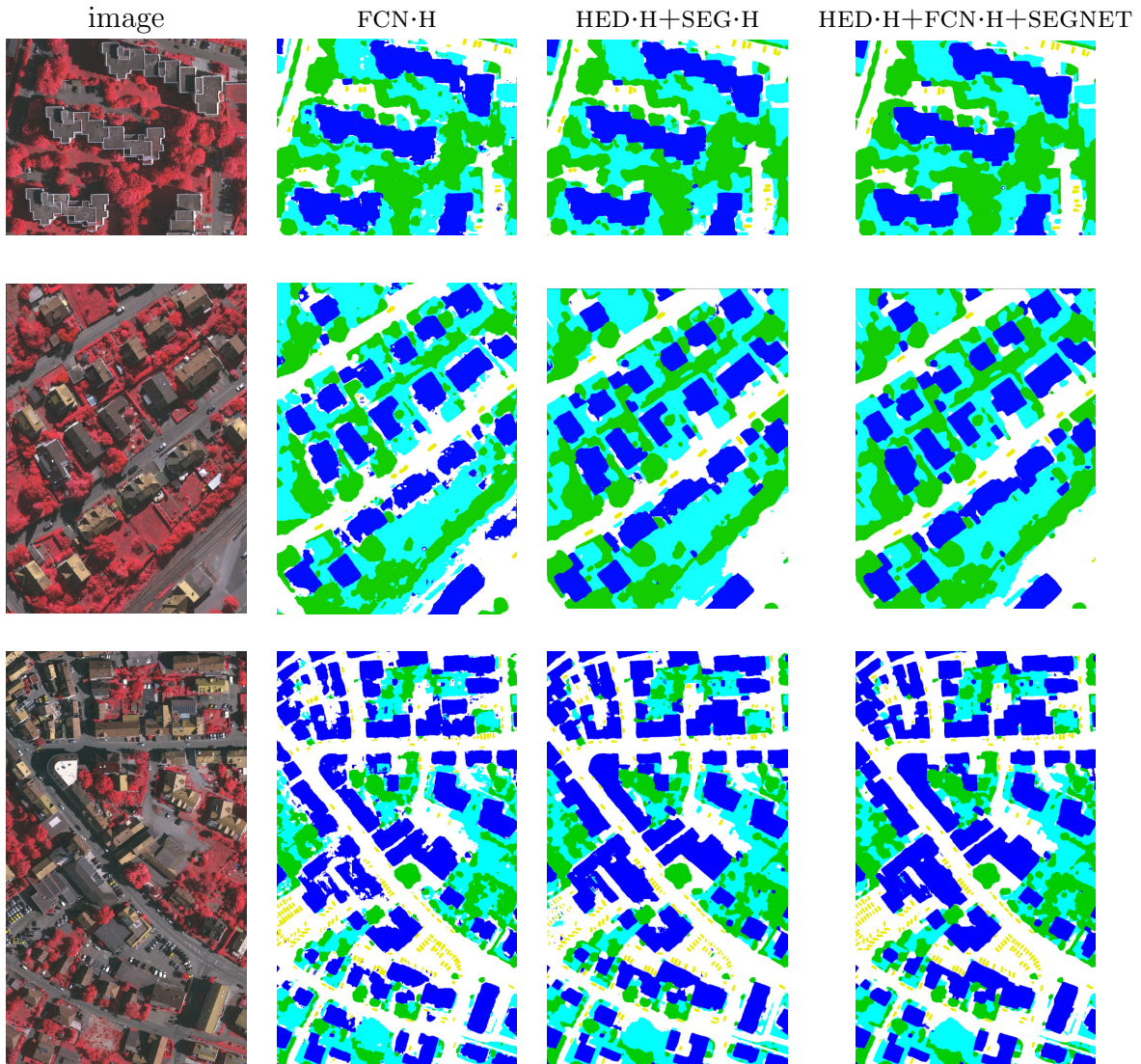


Figure 7: Example predictions on the official Vaihingen test set. The second to fourth column show the outputs of FCN·H (DLR\_1), HED·H +SEGNET (DLR\_5) and HED·H +FCN·H +SEGNET (DLR\_7). **White:** Impervious Surfaces, **Blue:** Buildings, **Cyan:** Low-Vegetation, **Green:** Trees, **Yellow:** Cars.

Table 5: Confusion matrix of our best result (*DLR\_9*) on the private Vaihingen test set. Values are percent of predicted pixels (rows sum to 100%, off-diagonal elements are false alarm rates).

|           |                   | reference         |                 |                |              |                |
|-----------|-------------------|-------------------|-----------------|----------------|--------------|----------------|
|           |                   | <i>Impervious</i> | <i>Building</i> | <i>Low-Veg</i> | <i>Tree</i>  | <i>Car</i>     |
| predicted | <i>Impervious</i> | <b>93.2 %</b>     | 2.2 %           | 3.6 %          | 0.9 %        | 0.1 %          |
|           | <i>Building</i>   | 2.8 %             | <b>95.3 %</b>   | 1.6 %          | 0.3 %        | 0.0 %          |
|           | <i>Low-Veg</i>    | 3.7 %             | 1.4 %           | <b>82.5 %</b>  | 12.5 %       | 0.0 %          |
|           | <i>Tree</i>       | 0.7 %             | 0.2 %           | 6.9 %          | <b>92.3%</b> | 0.0 %          |
|           | <i>Car</i>        | 19.5 %            | 7.0 %           | 0.5 %          | 0.4 %        | <b>72.60 %</b> |
|           | <i>Precision</i>  | 91.6 %            | 95.0 %          | 85.5 %         | 87.5 %       | 92.1 %         |
|           | <i>Recall</i>     | 93.2 %            | 95.3 %          | 82.5 %         | 92.3%        | 72.6 %         |
|           | <i>F1-score</i>   | 92.4 %            | 95.2 %          | 83.9 %         | 89.9 %       | 81.2 %         |

significant definition uncertainty and we could not ensure to use exactly the same definitions as the original annotators.

We then evaluate the new annotation, the ground truth from the benchmark, and the output of our best model, against each other. Results are shown in Table 8. One can see significant differences, especially for the *cars* which are small and have a large fraction of pixels near the boundary. Considering the saturating progress on the benchmark (differences between recent submissions are generally < 2%) there is a very real danger that annotation errors influence the results and conclusions. It may be surprising, but the Vaihingen dataset (and seemingly also the Potsdam dataset) is reaching its limits after barely 3 years of activity. This is a very positive and tangible sign of progress, and a strong argument in favor of public benchmarks. But it is also a message to the community: if we want to continue using benchmarks – which we should – then we have to make the effort and extend/renew them every few years. Ideally, it may be better to move to a new dataset altogether, to avoid overfitting and ensure state-of-the-art sensor quality.

Table 6: Short names of our model variants on the ISPRS Vaihingen 2D benchmark website.

| <i>Abbreviation</i> | <i>Model Details</i>                    |
|---------------------|---|
| DLR_1               | FCN·H                                   |
| DLR_2               | FCN·H+CRF                               |
| DLR_3               | HED·H+FCN·H                             |
| DLR_4               | HED·H+FCN·H+CRF                         |
| DLR_5               | HED·H+SEGNET                            |
| DLR_6               | HED·H+SEG·H+CRF                         |
| DLR_7               | HED·H+FCN·H+SEG·H                       |
| DLR_8               | HED·H+FCN·H+SEG·H+CRF                   |
| DLR_9               | HED·H+FCN·H+SEG·H, nDSM corrections     |
| DLR_10              | HED·H+FCN·H+SEG·H+CRF, nDSM corrections |

Table 7: Per-class  $F_1$ -scores and overall accuracies of top performers on the Vaihingen benchmark (numbers copied from benchmark website). DLR\_7 is our ensemble model, DLR\_9 is our ensemble with corrected nDSM. Acronyms are taken from the official ISPRS-Vaihingen website.

|       | <i>Impervious</i> | <i>Building</i> | <i>Low-Veg</i> | <i>Tree</i>   | <i>Car</i>    | <i>OA</i>     |
|-------|-------------------|-----------------|----------------|---------------|---------------|---------------|
| DST_2 | 90.5 %            | 93.7 %          | 83.4 %         | 89.2 %        | 72.6 %        | 89.1 %        |
| INR   | 91.1 %            | 94.7 %          | 83.4 %         | 89.3 %        | 71.2 %        | 89.5 %        |
| ONE_6 | 91.5 %            | 94.3 %          | 82.7 %         | 89.3 %        | <b>85.7 %</b> | 89.4 %        |
| ONE_7 | 91.0 %            | 94.5 %          | <b>84.4 %</b>  | 89.9 %        | 77.8 %        | 89.8 %        |
| DLR_7 | 91.4 %            | 93.8 %          | 83.0 %         | 89.3 %        | 82.1 %        | 89.4 %        |
| DLR_9 | <b>92.4 %</b>     | <b>95.2 %</b>   | 83.9 %         | <b>89.9 %</b> | 81.2 %        | <b>90.3 %</b> |

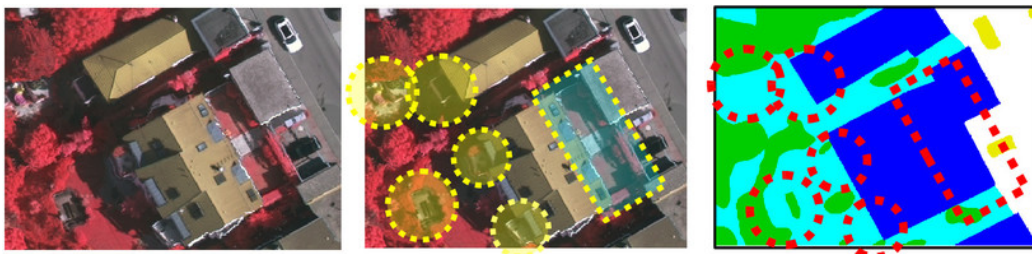


Figure 9: Examples of ground truth labeling errors. Yellow/red circles denote missing or incorrectly delineated objects.

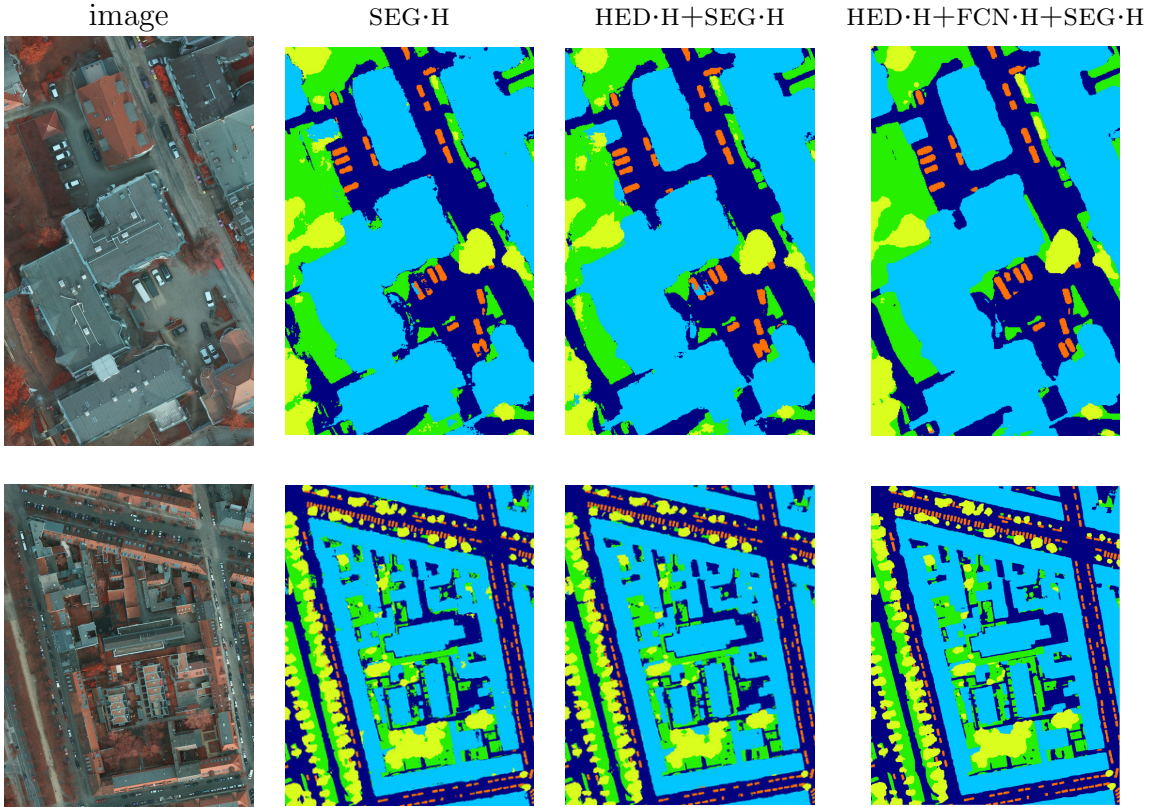


Figure 8: Example predictions on our Potsdam validation set. The second to fourth columns show results for SEG·H, HED·H+SEG·H and HED·H+FCN·H+SEG·H. **Dark Blue:** Impervious Surfaces, **Light Blue:** Buildings, **Green:** Low-Vegetation, **Yellow:** Trees, **Orange:** Cars.

## 5. Conclusion

We have developed DCNN models for semantic segmentation of high-resolution aerial images, which explicitly represent and extract the boundaries between regions of different semantic classes. Empirically, including class boundaries significantly improves different DCNN architectures, and was the single most important performance boost in our final model, which achieves excellent performance on the ISPRS Vaihingen and Potsdam benchmarks.

Moreover, we have presented an extensive study of semantic segmentation architectures, including presence or absence of fully connected layers, use of class boundaries, multi-scale processing, and multi-network ensembles.

Table 8: Inter-comparison between ISPRS Vaihingen ground truth, our own annotation, and our best models. Significant differences occur, suggesting that the benchmark may have to be re-annotated or replaced. See text for details.

|                 | HED·H +SEG·H- <i>Msc</i> |           | HED·H +FCN·H +SEG·H |           | benchmark label | our label       |
|-----------------|--------------------------|-----------|---------------------|-----------|-----------------|-----------------|
|                 | benchmark label          | our label | benchmark label     | our label | our label       | benchmark label |
| <i>Building</i> | 97.3 %                   | 97.8 %    | 97.7 %              | 98.0 %    | 97.9 %          | 94.7 %          |
| <i>Car</i>      | 84.6 %                   | 88.1 %    | 79.8 %              | 83.3 %    | 93.2 %          | 88.8 %          |

One aspect that we have not yet investigated, but that might be needed to fully exploit the information in the segmentation boundaries, are class-specific boundaries. Our current boundaries are class-agnostic, they do not know which classes they actually separate. It appears that this information could be preserved and used. Pushing this idea to its extremes, it would in fact be enough to detect *only* the class boundaries, if one can ensure that they form closed regions.

Although DCNNs are the state-of-the-art tool for semantic segmentation, they have reached a certain degree of saturation, and further improvements of segmentation quality will probably be small, tedious, and increasingly problem-specific. Nevertheless, there are several promising directions for future research. We feel that model size is becoming an issue. Given the excessive size and complexity of all the best-performing DCNN models, an interesting option would be to develop methods for compressing large, deep models into smaller, more compact ones for further processing. First ideas in this direction have been brought up by [Hinton et al. \(2015\)](#).

## References

### References

- Audebert, N., Le Saux, B., Lefèvre, S., 2016. Semantic segmentation of earth observation data using multimodal and multi-scale deep networks. In: Asian Conference on Computer Vision. Springer, pp. 180–196.
- Badrinarayanan, V., Kendall, A., Cipolla, R., 2017. Segnet: A deep convolutional encoder-decoder architecture for scene segmentation. IEEE transactions on pattern analysis and machine intelligence.
- Barndt, M. J., Barr, S. L., 1996. Inferring urban land use from satellite sensor images using kernel-based spatial reclassification. Photogrammetric Engineering and Remote Sensing 62 (8), 949–958.

- Bertasius, G., Shi, J., Torresani, L., 2015. High-for-low and low-for-high: Efficient boundary detection from deep object features and its applications to high-level vision. In: Proceedings of the IEEE International Conference on Computer Vision. pp. 504–512.
- Bischof, H., Schneider, W., Pinz, A. J., 1992. Multispectral classification of landsat-images using neural networks. *IEEE Transactions on Geoscience and Remote Sensing* 30 (3), 482–490.
- Chen, L., Papandreou, G., Kokkinos, I., Murphy, K., Yuille, A. L., 2016a. Deeplab: Semantic image segmentation with deep convolutional nets, atrous convolution, and fully connected crfs. *CoRR* abs/1606.00915.
- Chen, L.-C., Barron, J. T., Papandreou, G., Murphy, K., Yuille, A. L., 2016b. Semantic image segmentation with task-specific edge detection using cnns and a discriminatively trained domain transform. In: Proceedings of the IEEE Conference on Computer Vision and Pattern Recognition. pp. 4545–4554.
- Chen, L.-C., Papandreou, G., Kokkinos, I., Murphy, K., Yuille, A., May 2015. Semantic Image Segmentation with Deep Convolutional Nets and Fully Connected CRFs. In: International Conference on Learning Representations. San Diego, United States.
- Dai, J., He, K., Sun, J., 2016. Instance-aware semantic segmentation via multi-task network cascades. In: Proceedings of the IEEE Conference on Computer Vision and Pattern Recognition. pp. 3150–3158.
- Dalla Mura, M., Benediktsson, J. A., Waske, B., Bruzzone, L., 2010. Morphological attribute profiles for the analysis of very high resolution images. *IEEE Transactions on Geoscience and Remote Sensing* 48 (10), 3747–3762.
- Dosovitskiy, A., Fischer, P., Ilg, E., Häusser, P., Hazırbaş, C., Golkov, V., v.d. Smagt, P., Cremers, D., Brox, T., 2015. FlowNet: Learning optical flow with convolutional networks. In: IEEE International Conference on Computer Vision (ICCV).
- Farabet, C., Couprie, C., Najman, L., LeCun, Y., 2013. Learning hierarchical features for scene labeling. *IEEE transactions on pattern analysis and machine intelligence* 35 (8), 1915–1929.

- Franklin, S. E., McDermid, G. J., 1993. Empirical relations between digital SPOT HRV and CASI spectral response and lodgepole pine (*pinus contorta*) forest stand parameters. International Journal of Remote Sensing 14 (12), 2331–2348.
- Fu, K. S., Landgrebe, D. A., Phillips, T. L., 1969. Information processing of remotely sensed agricultural data. Proceedings of the IEEE 57 (4), 639–653.
- Gal, Y., Ghahramani, Z., 2016. Dropout as a bayesian approximation: Representing model uncertainty in deep learning. In: International Conference on Machine Learning. pp. 1050–1059.
- Gerke, M., 2014. Use of the stair vision library within the isprs 2d semantic labeling benchmark (vaihingen). Tech. rep., ITC, University of Twente.
- Glorot, X., Bengio, Y., 2010. Understanding the difficulty of training deep feedforward neural networks. In: International conference on Artificial Intelligence and Statistics (AISTATS).
- Grangier, D., Bottou, L., Collobert, R., 2009. Deep convolutional networks for scene parsing. In: ICML 2009 Deep Learning Workshop. Vol. 3. Citeseer.
- Hinton, G., Vinyals, O., Dean, J., 2015. Distilling the knowledge in a neural network. arXiv preprint arXiv:1503.02531.
- Kampffmeyer, M., Salberg, A.-B., Jenssen, R., 2016. Semantic segmentation of small objects and modeling of uncertainty in urban remote sensing images using deep convolutional neural networks. In: Proceedings of the IEEE Conference on Computer Vision and Pattern Recognition Workshops. pp. 1–9.
- Kokkinos, I., 2016. Pushing the boundaries of boundary detection using deep learning. In: International Conference on Learning Representations (ICLR).
- Krähenbühl, P., Koltun, V., 2011. Efficient inference in fully connected crfs with gaussian edge potentials. In: Advances in Neural Information Processing Systems.

- Längkvist, M., Kiselev, A., Alirezaie, M., Loutfi, A., 2016. Classification and segmentation of satellite orthoimagery using convolutional neural networks. *Remote Sensing* 8 (4), 329.
- Lee, C.-Y., Xie, S., Gallagher, P., Zhang, Z., Tu, Z., 2015. Deeply-supervised nets. In: *AISTATS*.
- Long, J., Shelhamer, E., Darrell, T., 2015. Fully convolutional networks for semantic segmentation. In: *Proceedings of the IEEE Conference on Computer Vision and Pattern Recognition*. pp. 3431–3440.
- Maggiori, E., Tarabalka, Y., Charpiat, G., Alliez, P., 2016. High-resolution semantic labeling with convolutional neural networks. *arXiv preprint arXiv:1611.01962*.
- Malmgren-Hansen, D., Nobel-J, M., et al., 2015. Convolutional neural networks for sar image segmentation. In: *2015 IEEE International Symposium on Signal Processing and Information Technology (ISSPIT)*. IEEE, pp. 231–236.
- Marcu, A., Leordeanu, M., 2016. Dual local-global contextual pathways for recognition in aerial imagery. *arXiv preprint arXiv:1605.05462*.
- Marmanis, D., Wegner, J., Galliani, S., Schindler, K., Datcu, M., Stilla, U., 2016. Semantic segmentation of aerial images with an ensemble of cnns. *ISPRS Annals of Photogrammetry, Remote Sensing and Spatial Information Sciences*, 473–480.
- Mayer, H., Hinz, S., Bacher, U., Baltsavias, E., 2006. A test of automatic road extraction approaches. *International Archives of Photogrammetry, Remote Sensing, and Spatial Information Sciences* 36 (3), 209–214.
- Mnih, V., Hinton, G. E., 2010. Learning to detect roads in high-resolution aerial images. In: *European Conference on Computer Vision*. Springer, pp. 210–223.
- Mou, L., Zhu, X., 2016. Spatiotemporal scene interpretation of space videos via deep neural network and tracklet analysis. In: *2016 IEEE International Geoscience and Remote Sensing Symposium (IGARSS)*. IEEE, pp. 4959–4962.

- Noh, H., Hong, S., Han, B., 2015. Learning deconvolution network for semantic segmentation. In: Proceedings of the IEEE International Conference on Computer Vision. pp. 1520–1528.
- Paisitkriangkrai, S., Sherrah, J., Janney, P., Hengel, V.-D., et al., 2015. Effective semantic pixel labelling with convolutional networks and conditional random fields. In: Proceedings of the IEEE Conference on Computer Vision and Pattern Recognition Workshops. pp. 36–43.
- Pinheiro, P., Collobert, R., 2014. Recurrent convolutional neural networks for scene labeling. In: International Conference on Machine Learning. pp. 82–90.
- Pinheiro, P. O., Lin, T.-Y., Collobert, R., Dollár, P., 2016. Learning to refine object segments. In: European Conference on Computer Vision. Springer, pp. 75–91.
- Richards, J. A., 2013. Remote sensing digital image analysis. Springer.
- Russell, B., Efros, A., Sivic, J., Freeman, B., Zisserman, A., 2009. Segmenting scenes by matching image composites. In: Advances in Neural Information Processing Systems. pp. 1580–1588.
- Saito, S., Yamashita, T., Aoki, Y., 2016. Multiple object extraction from aerial imagery with convolutional neural networks. Electronic Imaging 2016 (10), 1–9.
- Sherrah, J., 2016. Fully convolutional networks for dense semantic labelling of high-resolution aerial imagery. arXiv preprint arXiv:1606.02585.
- Simonyan, K., Zisserman, A., 2014. Very deep convolutional networks for large-scale image recognition. arXiv preprint arXiv:1409.1556.
- Socher, R., Huval, B., Bhat, B., Manning, C. D., Ng, A. Y., 2012. Convolutional-recursive deep learning for 3d object classification. In: Advances in Neural Information Processing Systems 25.
- Szeliski, R., 2010. Computer vision: algorithms and applications. Springer.
- Tokarczyk, P., Wegner, J. D., Walk, S., Schindler, K., 2015. Features, color spaces, and boosting: New insights on semantic classification of remote

- sensing images. *IEEE Transactions on Geoscience and Remote Sensing* 53 (1), 280–295.
- Volpi, M., Tuia, D., 2017. Dense semantic labeling of subdecimeter resolution images with convolutional neural networks. *IEEE Transactions on Geoscience and Remote Sensing* 55 (2), 881–893.
- Xie, S., Tu, Z., 2015. Holistically-nested edge detection. In: Proceedings of the IEEE International Conference on Computer Vision. pp. 1395–1403.
- Yang, J., Price, B., Cohen, S., Lee, H., Yang, M.-H., 2016. Object contour detection with a fully convolutional encoder-decoder network. In: Proceedings of the IEEE Conference on Computer Vision and Pattern Recognition. pp. 193–202.
- Yu, F., Koltun, V., 2016. Multi-scale context aggregation by dilated convolutions. In: International Conference on Learning Representations (ICLR).
- Zeiler, M. D., Fergus, R., 2014. Visualizing and understanding convolutional networks. In: European Conference on Computer Vision. Springer, pp. 818–833.